Analyses of Cryogenic Propellant Tank Pressurization based upon Experiments and Numerical Simulations

Carina Ludwig⋆ and Michael Dreyer⋆⋆
⋆DLR - German Aerospace Center, Space Launcher Systems Analysis (SART), Institute of Space Systems, 28359 Bremen, Germany, Carina.Ludwig@dlr.de
⋆⋆ZARM - Center for Applied Space Technology and Microgravity, University of Bremen, 28359 Bremen, Germany

Abstract

The active-pressurization of cryogenic propellant tanks for the launcher application was analyzed in this study. Therefore, ground experiments, numerical simulations and analytical studies were performed with the following important results: In order to minimize the required pressurant gas mass, a higher pressurant gas temperature is advantageous or the application of helium as pressurant gas. Numerical simulations of the pressurant gas mass using Flow-3D show good agreement to the experimental results. The dominating heat transfer during pressurization appears from the injected pressurant gas to the axial tank walls and the predominant way of phase change during the active-pressurization phase depends on the type of the pressurant gas. After the end of the pressurization phase, a significant pressure drop occurs. A theoretical model is presented for the analytical determination of this pressure drop.

Nomenclature

Roman letters

A	area
c_p	specific heat capacity at const. pressure
c_v	specific heat capacity at const. volume
D_t	thermal diffusion coefficient
H	fluid height
h	specific enthalpy
Δh_v	latent heat of evaporation
m	mass
R	tank radius
R_s	specific gas constant
r	radial coordinate
p	pressure
Δp	pressure drop
Q	heat
$\dot{Q}$	heat flow rate
T	temperature
t	time
U	internal energy
u	specific internal energy
v	velocity
z	height coordinate

Superscripts

*	nondimensional
$\bar{}$	mean

Greek letters

Θ	characteristic temperature difference
δ_T	thermal boundary layer thickness
λ	thermal conductivity
μ	dynamic viscosity
ρ	density

Subscripts

0	start
$cond$	condensation
f	end
i	initial
l	liquid
m	maximal
$relax$	relaxation
pg	pressurant gas
p	pressurization
$press$	pressurization
ref	reference
sat	saturation
T	relaxation end
v	vapor
w	wall
Γ	free surface

1. Introduction

Against the background of the new development of a European cryogenic upper stage for the new launcher generation, interest in the advancement of cryogenic fluid management technologies has been significantly revived. One part of the cryogenic fluid management system is the the tank pressurization system. The purpose of the pressurization system is to control and maintain the required pressure in the propellant tanks at any time of the mission. Therefore, a pressurant gas is injected into the propellant tank, which is usually evaporated propellant or an inert gas which is stored in additional vessels. Due to the very low temperatures of cryogenic fluids complex fluid-mechanic and thermodynamic processes occur during pressurization inside the propellant tank, which are not yet fully understood. Since launcher tank pressurization requires the use of on-board fluids, optimization of the pressurization process is essential in order to lower the launcher mass and therefore to increase the payload mass.
Experimental research in the field of active-pressurization had been pursued in the USA primarily during the Apollo missions. In 1962, Nein and Head [1] presented experimental data from the pressurized discharge of a full-scale Saturn liquid oxygen system, a large single liquid oxygen (LOX) tank and a small model liquid nitrogen (LN2) tank. They found that for the full-scale tanks, considerable mass transfer appears during expulsion between the gas in the tank ullage and the liquid propellant. The appearing mass transfer was always evaporation, except for the test, where the small model LN2 tank was pressurized with gaseous nitrogen (GN2), where condensation occurred during the entire discharge test. Furthermore, the major internal heat transfer was stated to take place between the ullage gas and the liquid surface and that the heat transfer between the ullage gas and the adjacent tank walls are of minor importance. However, the results for the small model tank indicated a reversal in the predominant mode of heat transfer.
Nein and Thompson [2] presented in 1966 experimental results for the pressurization of five large scale tank configurations. As results were summarized that no significant radial ullage temperature gradient occurs. The heat transfer between the vapor and tank walls can differ significantly from free convection, depending on the tank geometry and the diffuser design. However, the strongest influence on pressurant weight has the pressurant gas inlet temperature. An analysis of the mass transfer showed that condensation occurs for all of the evaluated test cases except for one test with a high pressurant gas inlet temperature.
Stochl et al. [3, 4, 5, 6] presented in 1969 and 1970 four reports on experimental investigations on the tank pressurization and expulsion of liquid hydrogen (LH2) from two different spherical tanks. Gaseous hydrogen and gaseous helium were used as pressurant gases. An increase of the inlet gas temperature results in a decrease in the pressurant requirement for constant ramp rates. Increasing the ramp rate results in a decrease in the pressurant requirement for constant inlet gas temperatures. Larger initial ullage volumes at constant ramp rates result in increased pressurant requirement. Increased ramp rates at given initial ullage volumes lead to decreased pressurant gas requirements. It was determined for all experiments that the inlet gas temperature has the strongest influence on the pressurant gas requirements, closely followed by the injector design.
In 1970, Lacovic [7] presented results of ramp and expulsion tests of a LOX tank similar to that of the Centaur stage, pressurized with helium. It was observed that the helium requirements increases with increasing tank ullage. No significant variation in helium requirements with ramp time appeared.
Van Dresar and Stochl [8] presented in 1993 experimental data of the pressurization and expulsion of a full-scale LH2 tank, pressurized with gaseous hydrogen (GH2). They stated that the mass transfer rate plays a significant role in ramp phases of practical duration. It was found that during a three minute ramp phase with a pressurant gas temperature of 280 K, mass transfer was not constant, but switches from evaporation to condensation and back to evaporation. Additionally it was stated that the pressurant requirements increases with increasing ramp time and the largest portion of the input energy goes into wall heating.
With the advancements in computing power and the enhancement of numerical simulation methods of the last decades, modeling of the propellant tank pressurization process has been extended with multidimensional computational techniques, such as CFD (computational fluid dynamics). Hardy and Tomsik [9] and Sasmal et al. [10] used the commercial CFD software Flow-3D for analyzes on the field of cryogenic tank pressurization and Adnani and Jennings [11] applied the commercial CFD code FLUENT. All studies however modeled only the tank ullage and therefore disregarded the phase change over the free surface and the associated heat transfer.
At the department of Space Launcher Systems Analysis (SART) at the DLR Institute of Space Systems, the in-house program PMP (Propellant Management Program) is used for the preliminary design of liquid propellant management systems for launcher and launcher related objects. PMP is a system analysis tool, which is used for preliminary design studies within a launch system context and is validated with data from existing launcher stages. Currently, PMP is reviewed and extended for the assessment of the more accurate sizing of the propellant tank pressurization systems for cryogenic stages. Proper predictions concerning the active-pressurization phase for cryogenic propellants for the launcher application require an improved understanding of the appearing complex fluid-dynamic and thermodynamic phenomena. The initial active-pressurization phase prior to engine ignition is therefore considered, as it represents

the preparatory phase which determines the initial conditions of the subsequent phases. Ground experiments were performed in a sub-scale propellant tank with liquid nitrogen as cryogenic model propellant, which was pressurized with gaseous nitrogen or gaseous helium. Numerical simulations were additionally performed, using the commercial CFD software Flow-3D and analytical approaches were applied. In this study, which is a continuation of the work already presented by Ludwig and Dreyer [12] in 2012, results of experiments, numerical simulations and theoretical approaches are described and conclusions drawn from these results are presented.

2. Experimental Set-Up

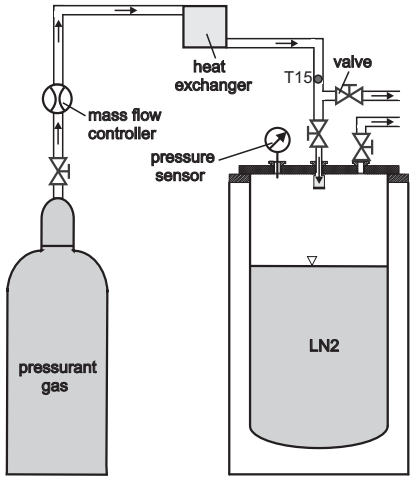

Figure 1: Drawing of the experimental set-up

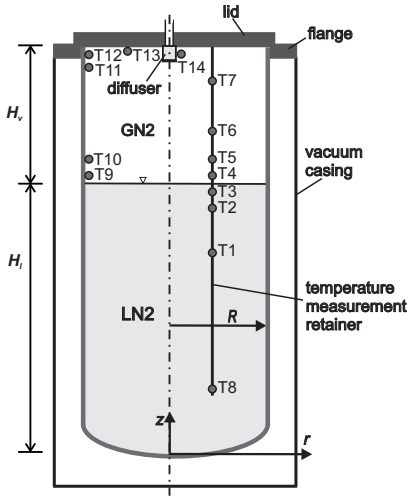

Figure 2: Experimental tank with locations of temperature sensors

In order to further understand the thermodynamic and fluid-dynamic phenomena during the initial active-pressurization process of cryogenic fluids, ground experiments were performed focusing on the initial active-pressurization process. For these experiments, liquid nitrogen (LN2) was used as a cryogenic propellant substitute, which was actively pressurized under normal gravity conditions up to different final tank pressures. As pressurant gases, gaseous nitrogen (GN2) and gaseous helium (GHe) were used with different inlet temperatures. The following section describes the experimental set-up and the test procedure.

The test facility used for this study is schematically depicted in Figure 1. It consisted of a storage bottle for the pressurant gas, a mass flow controller to ensure a constant pressurant gas mass flow, a heat exchanger to control the pressurant gas temperature and the high pressure tank, partly filled with liquid nitrogen, in which the active-pressurization took place and where the pressure was measured. Valves were used to control the flow. A more detailed view of the high pressure tank is depicted in Figure 2. It is a cylindrical test tank with a round shaped bottom placed in a vacuum casing for better insulation. In the top third of the tank, the inner wall is made of stainless steel with a thickness of $1.5{\cdot}10^{-3}$ m. The tank has an internal volume of 43 liter and was filled to two thirds with LN2. The liquid-vapor interface was at $z = H_l = 0.445$ m ($\pm$ $1{\cdot}10^{-3}$ m), the height of the tank ullage was $H_v = 0.205$ m ($\pm$ $1{\cdot}10^{-3}$ m) and the tank radius is $R = 0.148$ m. The temperature of the entering pressurant gas was measured at at temperature sensor (T15 in Figure 1) with an accuracy of $\pm$ 2.1 K. The pressurant gas was distributed in the tank by a diffuser, which is a sintered filter. The diffuser is sealed at the bottom so that the pressurant gas can only leave the filter radially, in order to protect the liquid surface from a direct jet.

The temperature inside the tank was logged at 14 positions with silicon diodes. The provider of the silicon diodes gives an accuracy for the sensors of $\pm$ 0.5 K, internal evaluation showed however that a higher accuracy of $\pm$ 0.1 K could be achieved for the performed experiments. The silicon diodes are marked in Figure 2 with black dots and Table 1 summarizes the exact positions in the tank. The temperature sensors T1 to T8 were arranged on a retainer in order to measure the temperature of the fluids. The sensors T1, T2, T3 and T8 were placed in the liquid nitrogen, sensors T4 to T7 in the tank ullage. The free surface was situated in the middle between the sensors T3 and T4. The sensors T9 to T12 measured the tank wall temperatures at different heights in the tank ullage and sensor T13 determined the temperature at the inner side of the lid. The temperature sensor T14 was placed next to the diffuser in order to log the temperature of the injected pressurant gas. A pressure sensor was located in the tank ullage to measure the tank pressure with an accuracy of $\pm$ 7.4 kPa. The pressurant gas mass flow was kept constant at 40 L_n/min for air (at 101.3 kPa and 273.15 K), which results in a maximum mass flow of $8.3{\cdot}10^{-4}$ kg/s for GN2 and $1.6{\cdot}10^{-4}$ kg/s for GHe.

In order to guarantee the same initial stratification conditions for each experiment run, the tank was filled with LN2

Table 1: Positions of the temperature sensors inside the tank. The error is ± 0.5·10^{-3} m.

sensor	T1	T2	T3	T4	T5	T6	T7	T8
r [m]	0.0980	0.0980	0.0980	0.0980	0.0980	0.0980	0.0980	0.0980
z [m]	0.330	0.430	0.440	0.450	0.460	0.510	0.610	0.110

sensor	T9	T10	T11	T12	T13	T14
r [m]	-0.1480	-0.1480	-0.1480	-0.1480	-0.0980	0.0063
z [m]	0.450	0.460	0.625	0.630	0.650	0.644

several hours before the start of the experiment. Evaporating nitrogen could leave through the tank outlet (see Figure 1). When the liquid surface reached the pre-defined position in the middle between the temperature sensors T3 and T4, indicated by a characteristic thermal stratification, the actual active-pressurization experiment was started. The outlet valve next to T15 was then opened and the feed lines from the pressurant gas storage bottle to the branching were chilled down. The tank outlet valve was then closed and the inlet valve opened. The tank was now pressurized as pressurant gas was fed into the tank. When the final tank pressure was reached, the inflow was stopped by closing the tank inlet valve of the tank so that no mass could enter or leave the tank. Inside the tank, relaxation took place. After a pre-set time, the tank outlet valve was opened again and the experiment was completed. During the whole experiment, the tank pressure and the temperatures were logged.
For this study, either GN2 or GHe was used as pressurant gas. For the GN2 experiments, four different pressurant gas temperatures T_{pg} were chosen, measured at T15 (see Figure 1), to reach three different final tank pressures p_f. For the GHe pressurization two pressurant gas temperatures with two final tank pressures were selected (see Table 2). The experiment N300aH was an exception as it had an increased liquid level to H_l = 0.455 m which results in a 5% smaller ullage volume.

Table 2: Experimental matrix and relevant results of the performed experiments.

Exp.	*press. gas*	T_{pg} [K]	p_f [kPa]	t_{press} [s]	t_{relax} [s]	p_f^* [ ]	Δp^* [ ]
N200r	GN2	144	200	27.0	59.9	1.89	0.29
N300r	GN2	144	300	79.9	331.3	2.83	0.56
N400r	GN2	144	400	155.2	-	3.78	-
N200c	GN2	263	200	24.1	55.5	1.89	0.35
N300c	GN2	263	300	60.9	178.9	2.83	0.53
N400c	GN2	263	400	96.8	241.0	3.78	0.68
N200a	GN2	294	200	25.5	55.2	1.89	0.33
N300a	GN2	294	300	64.3	148.3	2.83	0.51
N400a	GN2	294	400	100.1	251.9	3.78	0.66
N200h	GN2	352	200	23.6	64.1	1.89	0.36
N300h	GN2	352	300	60.7	152.3	2.83	0.53
N400h	GN2	352	400	60.7	152.3	3.78	0.69
N300aH	GN2	294	300	52.7	131.1	2.83	0.55
He200c	GHe	263	200	14.6	90.9	1.89	0.33
He400c	GHe	263	400	57.2	188.5	3.78	0.63
He200h	GHe	352	200	15.1	90.6	1.89	0.34
He400h	GHe	352	400	51.5	171.7	3.78	0.59

3. Numerical Model

For the numerical analysis of this study the commercial CFD program Flow-3D version 10.0 was used. It is a general purpose CFD code which numerically solves the equations of motion for fluids to determine transient, three-dimensional solutions to multi-scale, multi-physics flow problems. For this study the experiment tank was modeled in a cylindrical coordinate system. The mesh was chosen as quasi 2-D cylindrical mesh with with an opening angle of 1° and the z-axis as plane of symmetry. The cell size was 0.002x0.0025 m and the used fluid properties at p = 101.3 kPa and T = 77.35 K were the following: for LN2 ρ_{LN2} = 806.11 kg/m^3, μ_{LN2} = 160.69·10^{-6} Pa s, $c_{v,LN2}$ = 1084.1 J/(kg K) and λ_{LN2} = 0.14478 W/(m K). And for GN2 ρ_{GN2} = 4.6096 kg/m^3, μ_{GN2} = 5.4436·10^{-6} Pa s and $R_{s,GN2}$ = 296.8 J/(kg K).

For helium: $R_{s,GHe}$ = 2077 J/(kg K) and $c_{v,GHe}$ = 3115.9 J/(kg K). For the performed simulations, phase change was considered with the saturation pressure p_{sat} = 101.3 kPa at T_{sat} = 77.35 K and the latent heat of evaporation of Δh_v = 199180 J/kg. The Flow-3D accommodation coefficient *rsize* was set to 0.1 for most of the experiments (see Table 3) and the exponent of the saturation curve was 0.0014 1/K [13]. The system was modeled using a two fluid model with a free surface under the consideration of gravity, fluid to solid heat transfer and the first order approximation of the density transport equation. The pressurant gas was brought into the tank by a mass source, placed at the position and with the dimensions of the diffuser. The pressurant gas mass flow rate for GN2 was $2.3{\cdot}10^{-6}$ kg/s and $0.5{\cdot}10^{-6}$ kg/s for GHe with the corresponding pressurant gas temperatures T_{pg} summarized in Table 2. If helium was used as pressurant gas, the non-condensable gas model was used. For both pressurant gases, the viscous laminar flow model was applied. An additional baffle had to be placed above the free surface with the porosity of 1 and no heat transfer properties. This was necessary for the simulations due to the fact that the free surface got otherwise disturbed by the pressurant gas flow. It was found however, that during the performed experiments the free surface was not affected by the pressurant gas flow.
The lid of the experimental tank had a constant outside temperature of 280 K. The initial state for the simulations was: LN2 had a liquid temperature of 77 K and the vapor phase was thermally stratified, using the data from the initial temperature profile of the experiments. The tank wall had the same initial temperature as the fluids. For the thermal conductivity of the tank walls, temperature dependent data according to Barron [14] were applied. The initial tank pressure was taken from the experimental data and the implicit pressure solver GMRES was selected. Please note that in contrast to previous numerical pressurization studies mentioned in the introduction the results presented in this study included the simulation of the heat and mass transfer over the free surface.

4. Experimental, Numerical and Analytical Results

In the following chapter, the main results of the performed active-pressurization experiments are presented together with results from numerical simulations and theoretical approaches.

4.1 Data Scaling

The experimental data in this paper is presented in nondimensional form in order to be able to compare the achieved results to other experimental data or fluids. The nondimensional liquid temperature is therefore defined as:

$$T_l^* = \frac{T_l - T_{ref}}{\Theta_l} = \frac{T_l - T_{ref}}{T_{sat,f} - T_{ref}} \tag{1}$$

The temperature $T_{sat,f}$ is the saturation temperature corresponding to the final tank pressure, for e.g. 300 kPa as the final pressure $T_{sat,f}$ = 87.9 K. The reference temperature T_{ref} is the saturation temperature at norm pressure p_{norm} = 101.3 kPa, which for nitrogen is T_{ref} = 77.35 K.
The nondimensional vapor temperatures T_v^*, wall temperatures T_w^* and dimensionless pressurant gas temperatures T_{pg}^* are defined as

$$T_v^* = \frac{T_v - T_{ref}}{T_{pg,m} - T_{ref}};\ T_w^* = \frac{T_w - T_{ref}}{T_{pg,m} - T_{ref}};\ T_{pg}^* = \frac{T_{pg} - T_{ref}}{T_{pg,m} - T_{ref}} \tag{2}$$

where $T_{pg,m}$ is the maximum pressurant gas temperature, here $T_{pg,m}$ = 352 K.
The tank pressure p and the pressure drop Δp are scaled by the characteristic thermodynamic pressure

$$p^* = \frac{p}{\rho_{ref,v}\, R_s\, T_{ref}};\ \Delta p^* = \frac{\Delta p}{\rho_{ref,u}\, R_s\, T_{ref}} \tag{3}$$

where $\rho_{ref,v}$ = 4.61 kg/m^3 is the reference density of GN2 at norm pressure and $R_{s,GN2}$ = 296.8 J/(kg K) is the gas constant of GN2.
The nondimensional pressurant gas mass m_{pg}^* is defined by the required pressurant gas mass m_{pg} over the vapor mass in the tank ullage before pressurization $m_{v,0}$ = 0.035 kg. The value for $m_{v,0}$ = 0.035 kg is the average over all experiments with a liquid height of H_l = 0.445 m. For the N300aH experiment, which had an increased liquid level $m_{v,0}$ = 0.032 kg. Every other vapor mass is scaled in the same way:

$$m_{pg}^* = \frac{m_{pg}}{m_{v,0}};\ m_v^* = \frac{m_v}{m_{v,0}} \tag{4}$$

The nondimensional time t^* is defined for this study as

$$t^* = t\,\frac{D_t}{A_\Gamma} \tag{5}$$

with D_t as the thermal diffusion coefficient of LN2 at norm pressure $D_t = 8.798{\cdot}10^{-8}$ m^2/s and A_Γ as the area of the liquid surface $A_\Gamma = 0.688$ m^2.

4.2 Pressure and Temperature Evolution

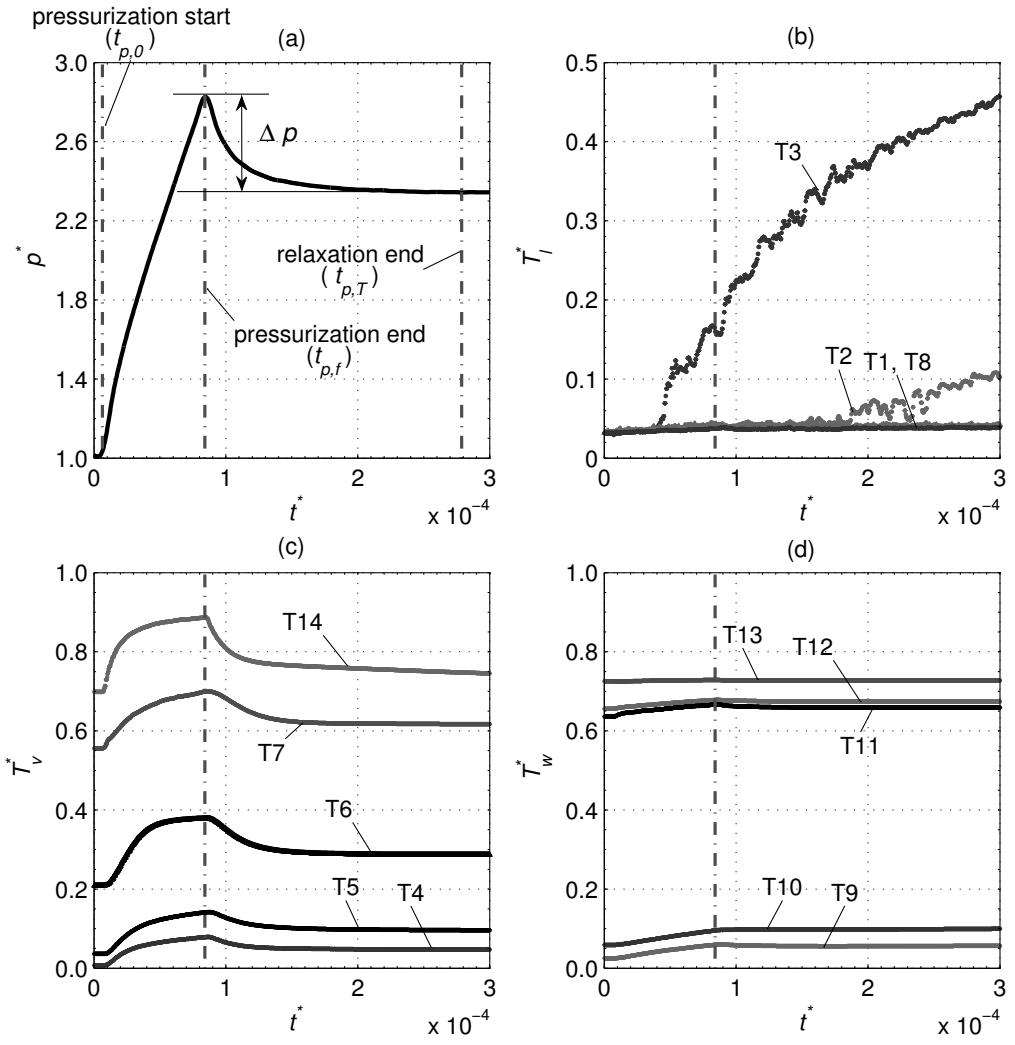

Figure 3: Non-dimensional (a) tank pressure, (b) liquid temperatures, (c) vapor temperatures, (d) wall and lid temperatures during pressurization and relaxation of the N300h experiment (for details see Table 2). T14 is the pressurant gas temperature at the diffuser. Pressurization starts at $t_{p,0}$ ($t^* = 0.06{\cdot}10^{-4}$) and ends at $t_{p,f}$ ($t^* = 0.84{\cdot}10^{-4}$). Relaxation takes place until $t_{p,T}$ ($t^* = 2.79{\cdot}10^{-4}$) and Δp is the characteristic pressure drop.

Before pressurization started, the tank ullage was filled only with evaporated nitrogen. The average initial tank pressure of all performed experiments was 106 kPa, the lid had always an outer temperature of 280 K and due to its construction a constant inner lid temperature of 278 K. The temperature of the free surface of the liquid is always considered to be the saturation temperature of the current tank pressure (Baehr and Stephan [18]). Figure 3 depicts pressure and temperature evolution of the pressurization experiment N300h. This experiment was pressurized with GN2 with a pressurant gas inlet temperature of 352 K (measured at T15, see Figure 1) and the final tank pressure of 300 kPa. During the pressurization phase, the tank pressure (Figure 3 (a)) increased almost linearly from pressurization start ($t_{p,0}$) to pressurization end ($t_{p,f}$). After the pressurization end, no more gas was injected and the tank pressure curve decreased asymptotically to a minimum pressure at relaxation end ($t_{p,T}$). The amount of the pressure drop is referred to as Δp. Figure 3 (b) depicts the evolution of the liquid temperatures. In the considered time frame, only the two uppermost temperature sensors T3 and T2 detected a change in temperature, whereas the bulk temperature (sensors T1 and T8) remained constant. The topmost sensor T3 traced the main temperature increase after the end of pressurization and the liquid temperature at T2 rose even later and with a weaker slope. In the vapor temperature evolution (Figure 3 (c)), the influence of the hot pressurant gas on the stratification during the pressurization process can be seen. The hot

pressurant gas increased the temperature of the vapor with decreasing impact from the lid downwards. After the end of the pressurization, the temperatures reduced analogously to the pressure. The pressurant gas temperature at sensor T14 was not constant over time since the connecting pipe between the tank inlet valve and the diffuser has to adapt to the gas temperature as it could not be chilled down before the pressurization. The wall temperatures (Figure 3 (d)) were also affected by the pressurization process, but much less than the vapor temperatures due to the slow reaction of the wall material. It can be seen that the lid temperature T13 was not changing over time.

4.3 Required Pressurant Gas Mass

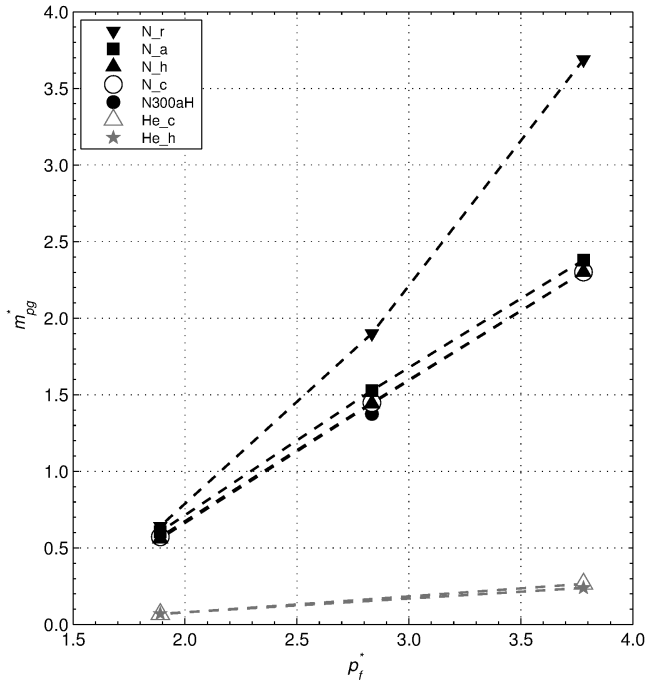

Figure 4: Non-dimensional required pressurant gas mass m_{pg}^{*} for all experiments over the nondimensional final tank pressure p_f^{*}. The dashed lines are only for better visualization.

One objective of this study was to investigate the required pressurant gas mass for a defined tank pressure raise. The required pressurant gas mass was therefore calculated by the pressurant gas mass flow multiplied with the needed pressurization time t_{press} (summarized in Table 2). Figure 4 shows the required pressurant gas masses for all performed experiments over the final tank pressure in nondimensional form. For better comparison, the GHe pressurized experiments were scaled with the same characteristic thermodynamic pressure as the GN2 experiments. The experiments with the same pressurant gas temperatures are merged in Figure 4 using one symbol, e.g. N200r, N300r and N400r are depicted as N_r. It can be nicely seen that the GN2 experiments with the lowest pressurant gas temperature N_r (T_{pg} = 144 K) had the highest pressurization times (see Table 2) and required therefore the most pressurant gas mass. The N_c experiments (T_{pg} = 263 K) required only little more pressurant gas mass then the N_h experiments which had the highest pressurant gas temperature (T_{pg} = 352 K). The helium experiments He_c and He_h showed the same characteristics. The interesting fact is that the N_a experiments with the inlet temperature of T_{pg} = 294 K needed more pressurant gas mass than the N_c experiments with a lower inlet temperature. This is due to the fact that for all experiments the pipe between the tank inlet valve and the diffuser had to be warmed up or cooled down to the pressurant gas inlet temperature. As the lid and therefore also the inlet pipe had an initial average temperature of 278 K, the inlet pipe had to be cooled down only a few degrees to adapt to the pressurant gas temperature of 263 K. Therefore, less pressurant gas mass was required than expected for the N_c experiments. It can moreover be seen that the required pressurant gas mass had a nearly linear correlation to the final tank pressure.
By comparison of the pressurization times t_{press} in Table 2, it can be seen that all helium pressurized experiments had very short pressurization times and Figure 4 shows that they therefore required much less pressurant gas than the corresponding GN2 experiments. This is due to the fact that helium has a very low molecular weight which results in general in a low fluid mass and the GHe pressurizations were much faster than the corresponding GN2 experiments. The faster pressurization happened on the one hand because helium cannot condense into LN2 during pressurization process and on the other hand because it has a much lower density than nitrogen, which means that less GHe was

Table 3: Experimental and numerical pressurant gas masses.

	Exp. [kg]	Flow-3D [kg]	error [%]	abs. error [kg]	*rsize* [ ]
N200c	0.0201	0.0216	7.9	0.0016	0.1
N300c	0.0507	0.0516	1.8	0.0009	0.1
N400c	0.0806	0.0807	0.2	0.0002	0.1
N200a	0.0212	0.0216	2.0	0.0004	0.1
N300a	0.0535	0.0516	-3.6	-0.0019	0.1
N400a	0.0833	0.0849	1.9	0.0016	0.1
N200h	0.0196	0.0208	5.9	0.0012	0.1
N300h	0.0505	0.0499	-1.2	-0.0006	0.1
N400h	0.0806	0.0799	-0.8	-0.0007	0.1
N200r	0.0225	0.0333	48.1	0.0108	0.1
N300r	0.0665	0.0707	6.4	0.0042	0.1
N400r	0.1292	0.1082	-16.2	-0.0209	0.1
N300aH	0.0439	0.0416	-5.1	-0.0022	0.1
He200c	0.0024	0.0013	-45.2	-0.0011	0.0001
He400c	0.0093	0.0068	-26.6	-0.0025	0.0001
He200h	0.0025	0.0005	-80.1	-0.0020	0.0001
He400h	0.0084	0.0029	-65.0	-0.0054	0.0001

needed to fill the tank ullage.
The pressurization phases were calculated using Flow-3D and Table 3 compares the required pressurant gas masses of the experiments and of the Flow-3D simulations with the corresponding errors. For all experiments, the pressurization phases could be simulated except for the N400r experiment, for which the simulation was always aborted before 400 kPa tank pressure was reached. The column with the relative errors shows that for the GN2 pressurized simulations with two exceptions a maximal error of 8% was achieved, which shows a good agreement. The two exceptions are the N200r and the N400r experiments which have the lowest pressurant gas temperature. For these experiments, the numerical pressure curve increases almost linearly, the experimental pressure increase however, has a more curved evolution. The GHe pressurized simulations show even higher errors. On one hand this is due to the fact that the pressurant gas masses were very small, as it can be seen in the absolute errors. On the other hand it is due to the more complex numerical computation of the gas mixture with a non-condensable gas in the vapor phase. In Flow-3D, an accommodation coefficient *rsize* has to be defined, which is a multiplier on the phase change rate. For the performed simulations, a *rsize* value of 0.1 was found to yield the best results for the simulation of the experimental pressure curve. For some simulations however, the Flow-3D accommodation coefficient *rsize* had to be reduced to enable simulation results (see Table 3). By reducing *rsize*, the phase change mass is decreased, which might be the reason that these simulations have the highest errors compared to the experimental values.

4.4 Phase Change

The phase change during the active-pressurization and the relaxation periods was analyzed. As it will later be shown, condensation predominates the pressurization and relaxation phases, the theoretical approach used hereafter is presented under the assumption of condensation as way of phase change. By assuming saturation temperature at the liquid surface, the vapor mass in the ullage for the GN2 experiments at pressurization start $m_{v,0}$, pressurization end $m_{v,f}$ and relaxation end $m_{v,T}$ could be calculated. It was therefore averaged over the internal energy using the experimental temperature data. With the pressurant gas masses m_{pg} presented in the previous section the condensed masses of GN2 from the pressurization start until the end of the pressurization $m_{cond,0,f}$ could be calculated with the conservation of mass $m_{cond,0,f} = m_{v,0} + m_{pg} - m_{v,f}$. The condensed mass of GN2 from the pressurization end until the end of the relaxation $m_{cond,f,T}$ was calculated as $m_{cond,f,T} = m_{v,f} - m_{v,T}$. For the helium pressurization only the vapor mass before pressurization could be calculated by averaging over the internal energy. Afterwards, the ullage was filled with GN2 and GHe. On that account, the amount of GHe in the tank ullage after pressurization start had to be determined by considering the vapor phase as an ideal gas mixture and assumed that no helium was dissolved in the liquid phase. For the calculation of the vapor masses $m_{v,f}$ and $m_{v,T}$ an estimation for the mean vapor temperature had to be used resulting in considerable errors, which were taken into account for the results presented hereafter. All results are displayed in Figure 5 in dimensionless form with the corresponding error bars. The GN2 in the tank ullage at pressurization start is depicted by the black bars ($m^*_{v,0}$). The nondimensional pressurant gas masses m^*_{pg} is depicted by the dark grey bars

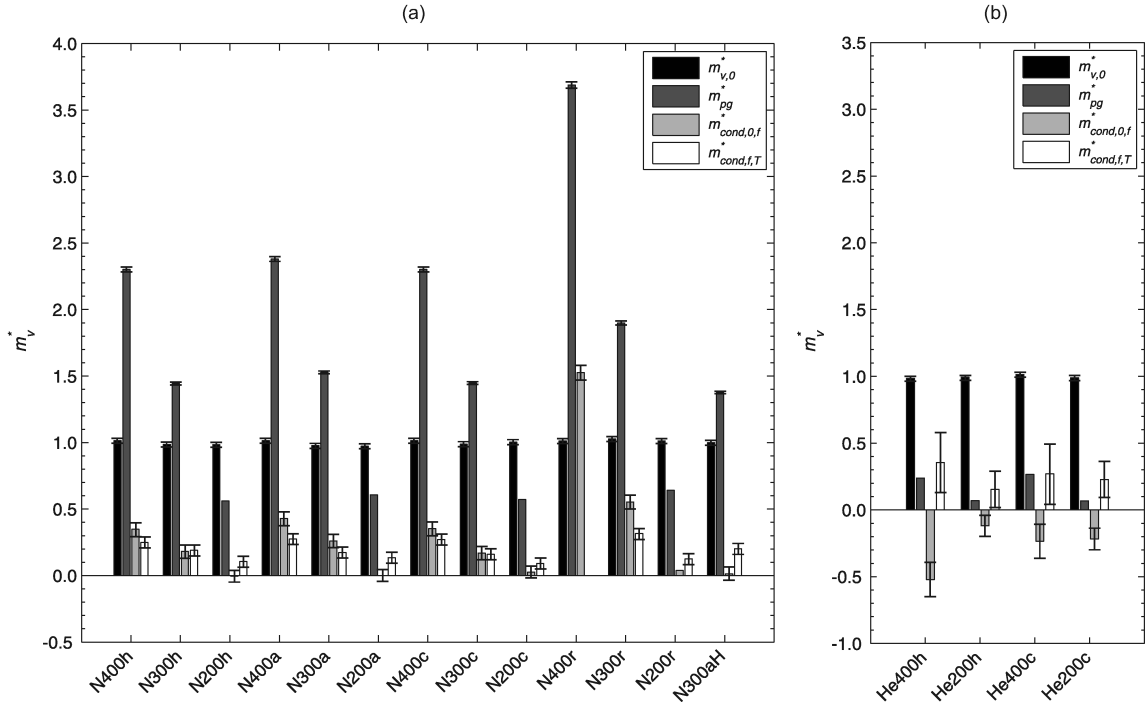

Figure 5: Nondimensional vapor mass at pressurization start ($m^*_{v,0}$), pressurant gas mass (m^*_{pg}), condensed vapor mass from pressurization start to pressurization end ($m^*_{cond,0,f}$) and condensed vapor mass from pressurization end to relaxation end ($m^*_{cond,f,T}$) for all GN2 (a) and the GHe (b) pressurized experiments with the relating errors.

and supports the data presented in the previous section: the longer the pressurization took, the higher was the required pressurant gas mass. For the GN2 pressurized experiments the amount of condensed GN2 from pressurization start until the pressurization end $m^*_{cond,0,f}$ (light grey bars in Figure 5 (a)) shows that the most GN2 condensed at the N400r experiment, which took the longest to reach the final tank pressure. For the N200h experiment, which had the shortest pressurization duration, the value for $m^*_{cond,0,f}$ is very small but negative, which means that this was the only experiment, for which evaporation dominated the phase change during pressurization. For the N200a experiment, $m^*_{cond,0,f}$ is nearly zero and for the N200c and N200r experiments, $m^*_{cond,0,f}$ has a small but positive values. It can also be seen that for the same pressurant gas temperatures, the amount of mass condensed during the pressurization phase increased with increasing final tank pressure which correlates with the increased pressurization time. The comparison of $m^*_{cond,0,f}$ for the N300a and the N300aH experiments, which only differed in the fluid level, shows a decrease in pressurization time of about 10 s for the N300aH experiment, which had a higher liquid level. This resulted in a noticeably lower amount of condensed GN2 during the pressurization phase. This leads to the conclusion, that during very short pressurization phases, evaporation dominates, and the longer the pressurization phases, the more condensation takes place. The reason for this might be the flow pattern of the pressurant gas: the injected GN2 flew from the diffuser downwards in the direction of the free surface. When the warm pressurant gas reached the cold liquid surface, it caused first evaporation, got then cooled down, enabling condensation.

The total amount of condensed GN2 from the pressurization end until the end of relaxation, which is characterized by a horizontal pressure evolution (see Figure 3 (a)), is depicted by the white bars in Figure 5. In Table 2, the corresponding relaxation times t_{relax} are summarized. For the N400r experiment, there is no data available for t_{relax} and $m^*_{cond,f,T}$ as the experiment had to be aborted before the relaxation end. In Figure 5 (a) it can be seen that condensation was the dominant method of phase change during the relaxation phase, even for the N200h experiment which had evaporation during the pressurization phase. The experiment with the highest amount of $m^*_{cond,f,T}$ was the N300r experiment, which also had the lowest pressurant gas temperature. It can be observed that the higher the final tank pressure was, the more GN2 condensed afterwards.

Figure 5 (b) shows the relevant masses for all four helium pressurized experiments. The GHe pressurant gas mass m_{pg} is depicted with dark grey bars. The condensed GN2 for the pressurization phase $m_{cond,0,f}$ had a negative value for all four experiments, which indicates that evaporation took place during the GHe pressurization phase. One explanation for this is that the specific heat capacity c_v of gaseous helium is about four times as high as that of gaseous nitrogen ($c_{v,GHe}$ = 3.1167·10^3 J/(kg K) and $c_{v,GN2}$ = 0.77127·10^3 J/(kg K) at p = 101.3 kPa and T = 77.35 K [15]). The injected

helium had still a quite high temperature when it reached the free surface and caused therefore evaporation. For the He400h experiment the most GN2 was evaporated, even though the required pressurant gas mass is very similar to that of the He400c experiment. This might be due to the fact that in this experiment a short pressurant gas jet occurred at the beginning of the pressurization due to a mistake in operating. A larger amount of GN2 evaporated therefore during the pressurization phase of the He400h experiment than would have been expected on the basis of the results of the other experiments. Condensed GN2 from pressurization end until relaxation end $m_{cond,f,T}$ is depicted for all four experiments with the white bars. It can be seen that, as for the GN2 pressurized experiments, condensation predominates during the relaxation phase.

4.5 Heat Transfer

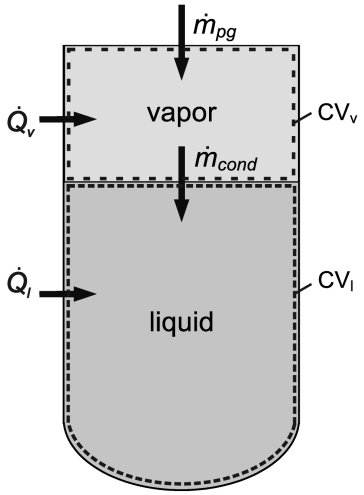

Figure 6: Schematical propellant tank with vapor and liquid phase, pressurant gas and condensation mass flow as well as the applied control volumes.

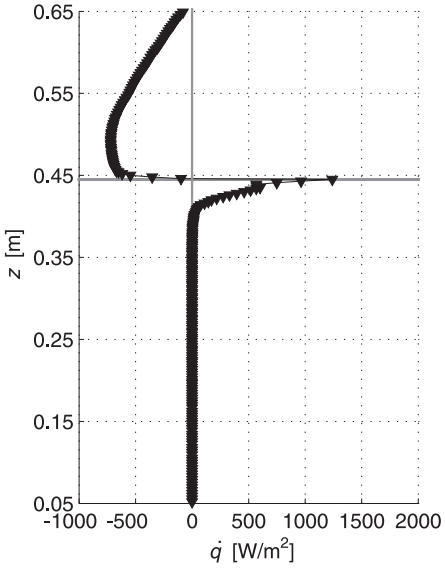

Figure 7: N300h experiment: wall to fluid heat flux at pressurization end ($t_{p,f}$) over the tank height.

In the following section, the analysis of the heat transfer during the active-pressurization and relaxation phases is presented. An energy balance was therefore applied to the pressure and temperature data of the experiments, and results of the numerical simulations for the wall to fluid heat flux are presented. The energy balance for the tank system is based on the first law of thermodynamics for open systems. Figure 6 schematically depicts the applied control volumes of the vapor (CV$_v$) and the liquid phase (CV$_l$), the pressurant gas mass flux m_{pg}, the condensation mass flux m_{cond} and the heat flows into the vapor phase $\dot{Q}_v$ and the liquid phase $\dot{Q}_v$. As condensation predominated the phase change, the first law of thermodynamics for open system takes the following form for the active-pressurization phase (index "$0,f$") of the liquid (for simplification evaporation was disregarded).

$$dQ_{l,0,f} = U_{l,f} - U_{l,0} - m_{cond,0,f}\, h_{v,cond,0,f} = m_{l,0}(u_{l,f} - u_{l,0}) + m_{cond,0,f}(u_{l,f} - h_{v,cond,0,f}) \tag{6}$$

The mass $m_{cond,0,f}$ is the condensed vapor mass from pressurization start until the pressurization end. $U_{l,f}$ is the internal energy of the total liquid at pressurization end and $U_{l,0}$ at the pressurization start. The final mass of the liquid $m_{l,f}$ can be written as $m_{l,f} = m_{l,0} + m_{cond,0,f}$. For the relaxation phase (index "f,T") follows accordingly

$$dQ_{l,f,T} = U_{l,T} - U_{l,f} - m_{cond,f,T}\, h_{v,cond,f,T} = m_{l,f}(u_{l,T} - u_{l,f}) + m_{cond,f,T}(u_{l,T} - h_{v,cond,f,T}) \tag{7}$$

where $m_{cond,f,T}$ is the liquid mass condensed from pressurization end until relaxation end. The specific internal energies u are determined using the NIST database [15] at the corresponding pressure and the average liquid temperature.
For the vapor phase, considering again only condensation, the first law of thermodynamics for open system takes the following form for the pressurization phase:

$$dQ_{v,0,f} = U_{v,f} - U_{v,0} - m_{pg}\, h_{pg} + m_{cond,0,f}\, h_{v,cond,0,f} = m_{v,0}(u_{v,f} - u_{v,0}) + m_{cond,0,f}(h_{v,cond,0,f} - u_{v,f}) + m_{pg}(u_{v,f} - h_{pg}) \tag{8}$$

Accordingly for the relaxation phase, the energy balance can be written as:

$$dQ_{v,f,T} = U_{v,T} - U_{v,f} + m_{cond,f,T}\, h_{v,cond,f,T} = m_{v,f}(u_{v,T} - u_{v,f}) + m_{cond,f,T}(h_{v,cond,f,T} - u_{v,T}) \tag{9}$$

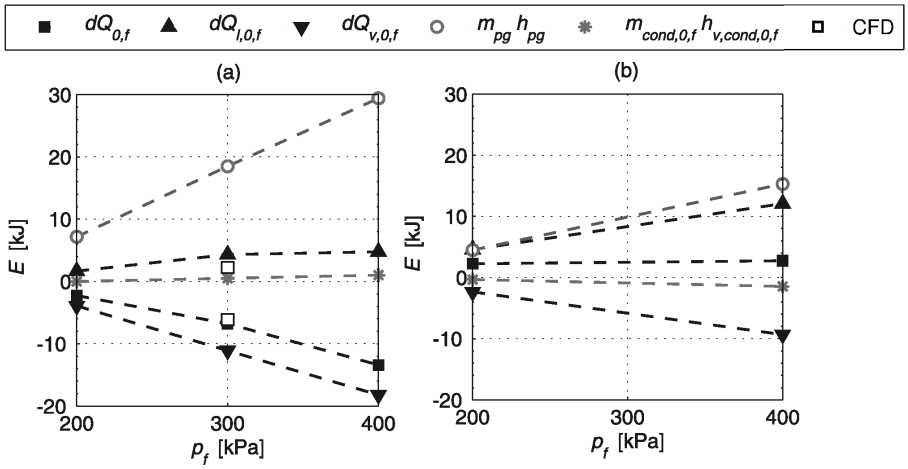

Figure 8: Energy balance of the pressurization phase of GN2 pressurized experiments: (a) N200h, N300h, N400h, (b) He200h, He400h. The dashed lines are only for better visualization.

For the experiments with GHe as pressurant gas, the specific internal energy of a gas mixture was used. With the conservation of energy, the change in the heat of the fluids for the pressurization phase and the relaxation phase were determined. In Figure 8 (a) the results of the energy balance from pressurization start until the pressurization end is depicted for three GN2 pressurized experiments. Figure 8 (b) shows the equivalent GHe pressurized experiments. The pressurant gas temperature was 352 K. The black squares represent the total change in heat of the test tank over the pressurization phase ($dQ_{0,f}$). This value can be split into the change in heat of the liquid ($dQ_{l,0,f}$) and the vapor phase ($dQ_{v,0,f}$). The amount of energy of the pressurant gas ($m_{pg}h_{pg}$) and the amount of energy, transferred from the vapor to the liquid phase by condensation $m_{cond,0,f}\ h_{v,cond,0,f}$ is shown. In Figure 8 (a), it can be seen that the change in heat for the total tank system $dQ_{0,f}$ has negative values. According to the definition of the signs, that amount of heat left the tank system during the pressurization phase. The results for the amount of energy transferred by condensation show that the amount of energy that enterd the liquid and left the vapor phase by phase change was very small. This leads to the conclusion, that during the pressurization period of the GN2 experiments, phase change has in general no major influence on the energy balance.

Comparatively, the energy of the pressurant gas $m_{pg}h_{pg}$ had a much bigger impact then the phase change on the energy balance. It primarily affected the vapor phase. The high amount of energy of the pressurant gas led to high, but negative values for the change in heat of the vapor phase $dQ_{v,0,f}$. This means, that the amount of energy brought into the system by the pressurant gas left the vapor phase very fast. As the amount of energy transferred over the free surface by condensation had no noticeable impact, it is assumed that the majority of the heat which was leaving the vapor phase, went into the tank wall and warmed it up.

Figure 7 depicts numerical results for the wall to fluid heat flux of the N300h experiment at pressurization end. It can be seen that in the region of the vapor phase (z = 0.445 m to z = 0.65 m) the heat went into the tank wall with increasing heat flux from the lid towards the free surface. Right below the free surface (z = 0.445 m) heat entered the liquid phase, also with decreasing amount in lateral direction. The referring data points for dQ_l and dQ_v are the white squares in Figure 8 (a). These results show that the heat entered the tank walls at the positions, where the largest temperature difference between the wall and the fluid appeared. By comparison of the numerical and the experimental results for dQ it can be seen that the simulation underestimates the amount of change in heat. However, based on Figure 7, it can be stated that the change in heat of the liquid phase $dQ_{l,0,f}$ was dominated by the heat entering from the wall. This also explains the positive sign of $dQ_{l,0,f}$ in Figure 8. If we recall the evolution of the tank wall temperatures of Figures 3 (d) it can be seen that all sensors T9 to T12 showed increasing wall temperatures over the pressurization period. As the lid temperature (T13) stayed constant over time, all heat which was leaving the vapor phase, entered the vertical tank walls. A small part of it was conducted down to the liquid phase, heating up the uppermost liquid layers.

Figure 8 (b) shows the energy balance for the pressurization phase of the helium pressurized experiments. The main difference between the change in heat for the GN2 and the GHe pressurization is the phase change: during the GN2 pressurization, condensation was the dominating way of phase change and for the helium pressurization it was evaporation. But, as already for the GN2 pressurization, also in this case the impact of the phase change on the energy balance was of minor importance. The energy of the pressurant gas $m_{pg}h_{pg}$ had the highest impact on the energy balance of the pressurization phase, dependent on the pressurant gas temperature. By comparing Figures 8 (a) and (b) it can be seen that the energy of the pressurant gas $m_{pg}h_{pg}$ for the GHe pressurized experiments was noticeably lower than that

of the GN2 pressurized experiments. This is due to the fact that the pressurant gas mass of the GHe experiments was much lower than that of the GN2 experiments. Moreover, the change in heat of the liquid phase was higher for the GHe experiments, as evaporation was the dominating way of phase change.
Figure 9 (a) depicts the energy balance of the relaxation phase for same GN2 pressurized experiments. For the relaxation period the amount of energy, transferred from the vapor to the liquid phase by condensation $m_{cond,f,T}\ h_{v,cond,f,T}$ had only little impact on the energy balance of the relaxation period. The vapor phase showed only few change in heat compared to the pressurization phase, as only a small amount of heat left the vapor phase and entered the tank wall. Figure 3 (d) shows the evolution of the wall temperature during the relaxation phase and it can be seen that the wall temperature decreased in the vapor phase over time. The heat, which entered the wall through the vapor phase during pressurization was conducted downwards to the liquid, resulting in a temperature decrease for the wall in the vapor phase. As the pressurization phases were very fast, the heat conduction still continued during the relaxation phase. It is assumed that the heat entered the liquid phase right below the free surface, warming up the uppermost liquid layers. Now heat conduction took also place in the liquid phase in a downward direction.
Figure 9 (b) displays the energy balance of the GHe pressurized experiments for the relaxation period. In contrast to the pressurization phase it can be seen that during the relaxation phase of the helium pressurized experiments, condensation was the predominating method of phase change. The energy of condensation $m_{cond,f,T}\ h_{v,cond,f,T}$ therefore has positive values, which are again very small. The change in heat of the vapor phase also indicates only a small heat transfer to the tank wall. As during the pressurization phase, less energy of the pressurant gas $m_{pg}h_{pg}$ was brought into the vapor phase compared to the GN2 experiments, and hence the change in heat for the liquid phase had smaller values compared to Figure 9 (a). Nevertheless, during the relaxation period the same effects of heat conduction through the wall were seen for the GHe pressurized experiments as for the GN2 experiments.

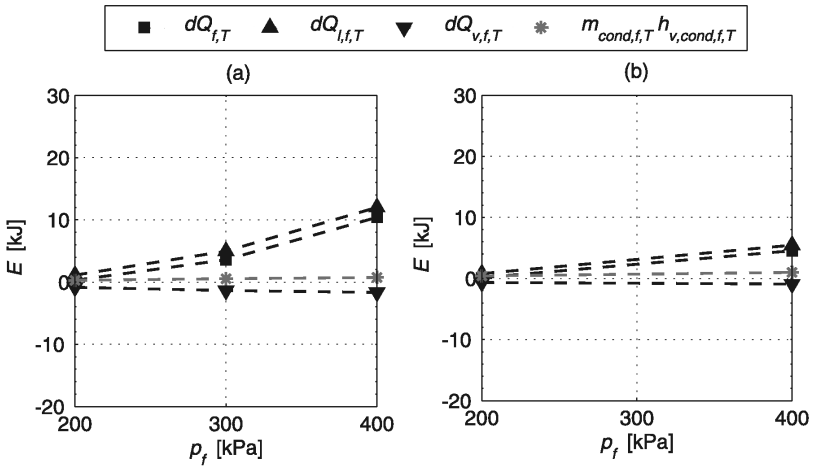

Figure 9: Energy balance of the relaxation phase of GN2 pressurized experiments: (a) N200h, N300h, N400h, (b) He200h, He400h. The dashed lines are only for better visualization.

4.6 Pressure Drop

During the active-pressurization experiments, the test tank was pressurized up to the final tank pressure. Then the pressurant gas inflow was stopped and the tank was let closed until the experiment was completed. As the pressurant gas inflow was stopped, the tank pressure decreased instantly and showed an asymptotical evolution until that point which is defined as relaxation end. Figure 3 (a) shows the evolution of the tank pressure during the N300h active-pressurization experiment for the pressurization phase and the relaxation phase. It can nicely be seen that the tank pressure dropped remarkably after the pressurization end but showed an asymptotical course to the end of the relaxation phase. The maximal pressure difference between the tank pressure at pressurization end and at relaxation end is defined as Δp. The pressure drop Δp is defined as the absolute value of the difference between the maximal tank pressure and the tank pressure at the relaxation end. In Figure 10, the dimensionless maximal pressure drop Δp^* over the dimensionless final tank pressure p_f^* is depicted for all performed experiments. The data for p_f^* and Δp^* are summarized in Table 2. It can be stated that the pressure drop Δp is in general linearly dependent on the final tank pressure. The gradient of the linear dependency however, is different for each pressurant gas temperature and species (GN2 or GHe). Also the ullage volume has an influence on Δp as it can be seen by comparison of the N300a and N300aH experiments.

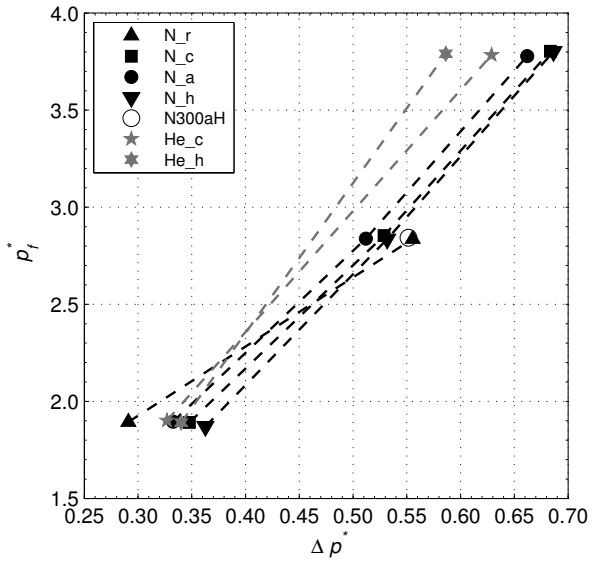

Figure 10: Nondimensional maximal pressure drop of the relaxation phase Δp^* over the dimensionless final tank pressure p_f^* for all performed experiments; dashed lines are only for better visualization.

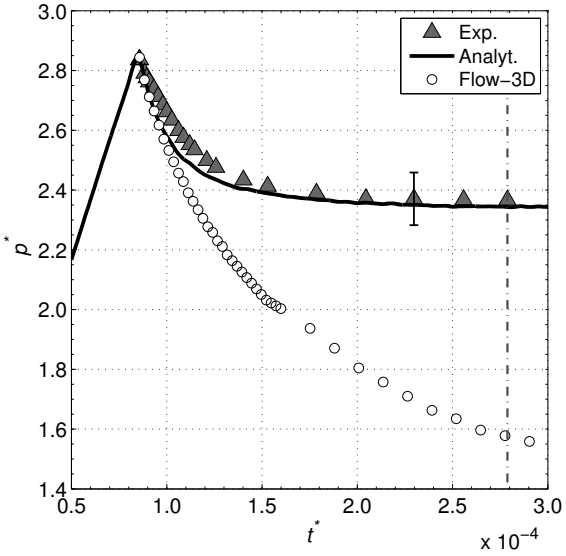

Figure 11: Experimental, numerical and analytical pressure drop with Equation (17) of the N300h experiment.

The gradient of the pressure drop was analyzed analytically with an equation, based on the pressure drop model for sloshing by Hopfinger and Das [16] and Das and Hopfinger [17] who presented an analytical analysis of the rate of pressure drop in a closed cylindrical container due to liquid sloshing. The analytical approach is based on the conservation of energy for the liquid phase under the assumption of incompressibility conditions and that the liquid velocity can be neglected and only a vertical temperature gradient has to be considered. With the thermal diffusivity D_t in a liquid being defined as $D_t = \lambda_l/(\rho_l\, c_{p,l})$ follows:

$$\frac{\partial T_l}{\partial t} = D_t\, \frac{\partial^2 T_l}{\partial z^2} \tag{10}$$

Integration from $z = 0$ to the liquid height H_l results in the following equation.

$$\frac{\partial}{\partial t} \int_0^{H_l} T_l\, dz = D_t\, \frac{\partial T_l}{\partial z}\bigg|_{z=H_l} = D_t\, \frac{\Theta}{\delta_T} \tag{11}$$

The thickness of the temperature gradient in the liquid due to thermal stratification is defined as the thermal boundary layer thickness δ_T. It can be determined analytically according to Baehr and Stephan [18] as $\delta_T = \sqrt{\pi D_t\, t}$ with the thermal diffusivity D_t and the time t. The heat flux at the interface per unit surface q_Γ is then derived from Fourier's law as

$$q_\Gamma = -\lambda_l \frac{\partial T_l}{\partial z}\bigg|_{z=H_l} = -\rho_l c_{p,l} D_t \frac{\partial T_l}{\partial z}\bigg|_{z=H_l} \tag{12}$$

and the associated condensation heat flux is $q_{\Gamma,cond} = v_{cond}\rho_{v,sat}\Delta h_v$ with the vapor density at saturation conditions $\rho_{v,sat}$ and the latent heat of evaporation Δh_v. With $q_\Gamma = q_{\Gamma,cond}$ and Equation 11, the vapor condensation velocity normal to the mean interface v_{cond} follows as

$$v_{cond}(t) = -\frac{D_t\, \rho_l(t)\, c_{p,l}(t)\, \Theta(t)}{\rho_{v,sat}(t)\, \Delta h_v(t)\, \delta_T(t)} = -\frac{D_t}{\delta_T(t)}\, \frac{\rho_l(t)}{\rho_{v,sat}(t)} \mathrm{Ja}(t) \tag{13}$$

where Ja is the Jakob number $\mathrm{Ja} = [c_{p,l}/\Delta h_v]\Theta$. The vapor phase is considered as an ideal gas here. Therefore, the pressure change in the system follows as

$$\frac{dp(t)}{dt} = \frac{R_s \bar{T}_{v,i}}{V_u} \frac{dm_v(t)}{dt} + \frac{p_i}{\bar{T}_{v,i}} \frac{d\bar{T}_v(t)}{dt} \tag{14}$$

where $\bar{T}_v$ is the ullage volume averaged mean vapor temperature, $\bar{T}_{v,i}$ is the initial mean vapor temperature and V_u is the ullage volume. The change of vapor mass is

$$\frac{dm_v(t)}{dt} = v_{cond}(t)\,\rho_{v,sat}(t)\,A_{cond}(t) + v_{evap}(t)\,\rho_{v,sat}(t)\,A_{evap}(t) \tag{15}$$

with A_{cond} as the area of the free surface where condensation takes place and A_{evap} where evaporation takes place with the evaporating vapor velocity v_{evap}. The pressure change as a function of time can be calculated using Equations 13, 14 and 15.

$$\frac{dp(t)}{dt} = \frac{R_s \bar{T}_{v,i}\,\rho_{v,sat}(t)}{V_u}\left(v_{evap}(t)A_{evap}(t) - \frac{\sqrt{D_t}\,\dfrac{\rho_{l,sat}(t)}{\rho_{v,sat}(t)}\,Ja(t)\,A_{cond}(t)}{\sqrt{\pi\,t}}\right) + \frac{p_i}{\bar{T}_{v,i}}\frac{d\bar{T}_v(t)}{dt} \tag{16}$$

Integration of Equation 16 from pressurization end $t_{p,f}$ to the time t results in the following

$$p(t) = p_f\,\frac{\bar{T}_v(t)}{\bar{T}_{v,p,f}} - \frac{R_s\,\bar{T}_{v,p,f}\,\rho_{v,sat}(t)}{V_u}\left[\frac{2\,\dfrac{\rho_{l,sat}(t)}{\rho_{v,sat}(t)}\,Ja(t)A_{cond}(t)\,\sqrt{D_{t,l}}}{\sqrt{\pi}}\left(\sqrt{t} - \sqrt{t_{p,f}}\right)\right] + \frac{R_s\,\bar{T}_{v,p,f}\,\rho_{v,sat}(t)}{V_u}\left[v_{evap}(t)A_{evap}(t)\,(t - t_{p,f})\right] \tag{17}$$

where Ja and ρ vary over time. As the evaporation velocity $v_{evap}(t)$, the condensation surface $A_{cond}(t)$ and the evaporation surface $A_{evap}(t)$ are not known. It is assumed that at the beginning of the relaxation phase condensation predominates and subsequently the amount of evaporated propellant increases. It is furthermore assumed that evaporation appears on an annular surface adjacent to the tank wall with increasing width. As the evolution over time of the width of this surface is not known, it is supposed for the analysis in this study that the evaporation and the condensation surface are half the area of the free surface over the whole relaxation phase $A_{cond}(t) = A_{evap}(t) = A_\Gamma/2$. The pressure drop due to evaporation is therefore probably overestimated and the pressure drop due to condensation underestimated. For the determination of the evaporation velocity $v_{evap}(t)$ the following assumption is made: At relaxation end it is supposed that the absolute values of the evaporation and condensation velocities are equal. On that account, the maximal value for the evaporation velocity $v_{evap}(t)$ in Equation 17 is chosen for the whole relaxation phase $|v_{evap}(t)| = |v_{cond}(t_{p,T})|$. The time t is the relaxation time starting at $t_{p,f}$ the peak of the pressure curve.

Figure 11 shows the results for the analytical approach compared to the experimental pressure data. The analytical pressure drop model described the initial pressure gradient very well. The asymptotical evolution was also covered. However, the tank pressure at relaxation end lay above the results of the theoretical approach, but still in the error margin (one errorbar is exemplarily depicted in Figure 11). The quite large error of the results of Equation 17 is due to the fact that for the theoretical approach the mean vapor temperature had to be determined. For this study, this was only feasible by averaging over the internal energy and assuming that between two temperature sensors the temperature distribution is linear. Moreover, the influence of evaporation on the tank pressure was only estimated, which also contributed to the error of the results of Equation 17. Please note that Equation 17 does not allow an a priori calculation of the pressure drop as the time dependent parameters have to be determined from the experimental data. However, the equation allows a better understanding of the driving factors of the pressure drop.

Figure 11 also depicts the Flow-3D calculation of the pressure drop. It is calculated with Flow-3D as a restart calculation from pressurization end and the mass source is therefore deactivated. It can be seen that a pressure drop occurs which fits very good the pressure evolution in the beginning of the pressure drop. Afterwards however, the pressure calculated by Flow-3D decreases much lower than that of the experiment. This is assumed to be due to the fact that the tank wall in the numerical model is only covered by on cell column, as the wall of the test tank has only a thickness of 0.0015 m. It might therefore result in a not very accurate resolution of the heat flows inside the wall, which might influence the pressure drop. If the numerical pressure evolution is considered after the experimental relaxation end, also a horizontal pressure curve appears but at a much lower pressure and therefore later than in the experiments. On that account, it can be summarized that the Flow-3D results of the pressure drop of the GN2 pressurized experiments can be used to determine the gradient of the pressure drop right after pressurization end, analyses at a later time however should not be performed based on this data. As the presented numerical model is designed with focus on the pressurization phase, other settings may be advantageous in order to further analyze the relaxation phase with Flow-3D. A finer resolution of the tank wall and therefore a more accurate consideration of the heat flow inside the tank wall might increase the accordance to the experimental pressure drop.

5. Conclusion

The objective of this paper was to improve the understanding of the thermodynamic and fluid-dynamic phenomena of cryogenic propellant tank pressurization for the launcher application. Therefore, ground experiments were performed using liquid nitrogen as model propellant in order to investigate the initial active-pressurization process. As pressurant gases, gaseous nitrogen and gaseous helium were analyzed at different inlet temperatures. The experimental set-up was described and the procedure for the experiments was presented. The evolution of the tank pressure and the temperatures in tank were investigated.
The required pressurant gas mass was determined experimentally with regard to the used pressurant gas and pressurant gas temperature. For the gaseous nitrogen pressurization an increased pressurant gas temperature decreased the required pressurant gas mass, as it was already stated by Stochl et al. [3, 4, 5, 6]. The reason for this, which was not mentioned by Stochl et al., is that for an increased pressurant gas temperatures the pressurization process is accelerated and therefore requires less pressurant gas mass. One exception was found in this study for the experiments where the pressurant gas temperature was near the initial temperature of the inlet pipe. For these experiments, less pressurant gas mass was required than expected as the heating respectively the cooling of the diffuser pipe also increases the pressurant gas need. In addition to an increased pressurant gas temperature, the use of helium as pressurant gas is also very advantageous as it cannot condense and has a low molecular weight and density. These results leads to the conclusion that the highest pressurant gas temperature needs the lowest pressurant gas mass, on condition that the pressurization lines are already chilled down in advance.
Additionally, numerical simulations using Flow-3D were performed also taking heat an mass transfer over the free surface into account. The results of the simulations showed a good agreement for the pressurization phase by comparison to the experimental results. For some experiments however, the Flow-3D accommodation coefficient *rsize* had to be decreased to enable a stable simulation, which decreased the mass transfer over the free surface and therefore also the accuracy of the numerical results.
As the dominating way of heat transfer during the pressurization phase, the heat transfer from the pressurant gas to the vertical tank walls was confirmed, as already stated by Nein and Head [1] for a small LN2 tank. The amount of heat transfer was found to be dependent on the temperature difference between the pressurant gas and the tank wall. The major way of the heat transfer into the liquid phase was the heat conducted from the warm tank walls downwards, entering the liquid phase right below the free surface. During the relaxation phase, the dominating way of heat transfer was the heat conducted from the warm tank walls downwards, entering the liquid phase. A thermal boundary layer appeared in the liquid with increasing thickness over time.
The mass involved in phase change during the pressurization and the relaxation phase was analytically determined based on experimental data. As results can be summarized that for the GN2 pressurized experiments, condensation was the dominating way of phase change during pressurization and relaxation phase. For the GHe pressurized experiments, evaporation occurred during the pressurization phase and condensation during the relaxation phase. One explanation for this is that the specific heat capacity c_v of gaseous helium is about four times as high as that of gaseous nitrogen. The injected helium had still a quite high temperature when it reached the free surface and caused therefore evaporation. Based on the experimental results of the short GN2 pressurization phases evaporation or hardly any phase change was determined. This might be due to the fact that the GN2 caused first evaporation when reaching the free surface and then got cooled down faster than the GHe, resulting in condensation for the longer pressurization phases. This assumption is reinforced by the statement of van Dresar and Stochl [8] that the mass transfer switches between evaporation and condensation in longer ramp phases.
Due to the condensation in the relaxation phase, which is due to the thermodynamic disequilibrium in the tank, a pressure drop occurred after the end of the active-pressurization phase. The tank pressure decreases and asymptotically approached a final pressure, defined as relaxation end, when the condensation and evaporation reached an equilibrium. The total amount of the pressure drop depended on the final tank pressure of the pressurization phase, the pressurant gas temperature and the fluid, applied as pressurant gas. An theoretical model was presented, which describes the evolution of the pressure drop. The results show that the phase change and the change in vapor temperature are the driving parameters of the pressure drop after pressurization end. The analysis of the pressure drop leads to the awareness that for a constant tank pressure, continuous pressurization of the propellant tanks is essential.

Acknowledgments

The authors acknowledge gratefully Peter Prengel, Frank Ciecior and Peter Friese for their effort in preparing and performing the experiments.

References

[1] M.E. Nein and R.R. Head. Experiences with pressurized discharge of liquid oxygen from large flight vehicle propellant tanks. In *Advances in Cryogenig Engineering*, vol. 7, New York, Plenum Press, 244–250.

[2] M.E. Nein and J.F. Thompson. Experimental and analytical studies of cryogenic propellant tank pressurant requirements: NASA TN D-3177, 1966.

[3] R.J. Stochl, J.E. Maloy, P.A. Masters and R.L. DeWitt. Gaseous-helium requirements for the discharge of liquid hydrogen from a 1.52-meter- (5-ft-) diameter spherical tank: NASA TN D-5621, 1970.

[4] R.J. Stochl, J.E. Maloy, P.A. Masters and R.L. DeWitt. Gaseous-helium requirements for the discharge of liquid hydrogen from a 3.96-meter- (13-ft-) diameter spherical tank: NASA TN D-7019, 1970.

[5] R.J. Stochl, P.A. Masters, R.L. DeWitt and J.E. Maloy. Gaseous-hydrogen requirements for the discharge of liquid hydrogen from a 1.52-meter- (5-ft-) diameter spherical tank: NASA TN D-5336, 1969.

[6] R.J. Stochl, P.A. Masters, R.L. DeWitt and J.E. Maloy. Gaseous-hydrogen requirements for the discharge of liquid hydrogen from a 3.96-meter- (13-ft-) diameter spherical tank: NASA TN D-5387, 1969.

[7] R.F. Lacovic. Comparison of experimental and calculated helium requirements for pressurization of a Centaur liquid oxygen tank: NASA TM X-2013, 1970.

[8] N.T. van Dresar and R.J. Stochl. Pressurization and expulsion of a flightweight liquid hydrogen tank: AIAA-93-1966, 1993.

[9] T.L. Hardy and T.M. Tomsik. Prediction of the ullage gas thermal stratification in a NASP vehicle propellant tank experimental simulation using Flow-3D: Nasa technical memorandum 103217, 1990.

[10] G.P. Samsal, J.I. Hochstein, M.C. Wendl and T.L. Hardy. Computational modeling of the pressurization process in a NASP vehicle propellant tank experimental simulation: AIAA 91-2407. *AIAA Joint Propulsion Conference and Exhibit*, 1991.

[11] P. Adnani and R.W. Jennings. Pressurization analysis of cryogenic propulsion systems: AIAA 2000-3788. In *36th AIAA/ASME/SAE/ASEE Joint Propulsion Conference & Exhibit, Huntsville, Alabama, USA, 2000*.

[12] C. Ludwig and M. Dreyer. Analyses of cryogenic propellant tank pressurization based upon ground experiments: AIAA 2012-5199. In *AIAA Space 2012 Conference & Exhibit, Pasadena, California, USA, 2012*.

[13] Flow Science Inc. Flow-3D User Manual - Version 10.0, 2011.

[14] R.F. Barron. Cryogenic heat transfer, 3. ed., Taylor & Francis, Philadelphia, 1999, p. 23

[15] E.W. Lemmon, M.L. Huber and M.O. McLinden. NIST Standard Reference Database 23: Reference Fluid Thermodynamic and Transport Properties-REFPROP, Version 9.0, National Institute of Standards and Technology, Standard Reference Data Program, Gaithersburg, 2010.

[16] E.J. Hopfinger and S.P. Das. Mass transfer enhancement by capillary waves at a liquid–vapour interface. *Experiments in Fluids*, Vol. 46, No.4: 597-605, 2009.

[17] S.P. Das and E.J. Hopfinger. Mass transfer enhancement by gravity waves at a liquid–vapour interface. *International Journal of Heat and Mass Transfer*, Vol. 52, No. 5-6: 1400-1411, 2009.

[18] H.D. Baehr and K. Stephan. Wärme- und Stoffübertragung, 6. ed., Springer, Berlin, 2008, p.491, p.302.